Physica Scripta. Vol. T109, 89–95, 2004

X-ray Magnetic Circular Dichroism for Quantitative Element-Resolved Magnetic Microscopy

Wolfgang Kuch*

Max-Planck-Institut für Mikrostrukturphysik, Weinberg 2, D-06120 Halle, Germany

Received May 3, 2003; accepted June 30, 2003

PACS ref: 75.70.Kw, 75.70.Ak

Abstract

The use of X-ray magnetic circular dichroism in the absorption of soft X-rays for the layer-resolved imaging of magnetic domains is introduced. A photoelectron emission microscope, used as position-sensitive detector for electron yield detection of resonant absorption of circularly polarized X-rays at elemental absorption edges, enables the imaging of the magnetic microstructures at surfaces and buried magnetic layers. Extended to full-image local X-ray magnetic circular dichroism microspectroscopy, this combination of techniques allows the local microscopic determination of element-resolved spin and orbital magnetic moments.

1. Introduction

After its first experimental verification in 1987 [1], X-ray magnetic circular dichroism (XMCD) in the absorption of soft X-rays has evolved into a widely used experimental tool for the element-specific characterization of magnetic properties. Several reasons can be cited for XMCD becoming so popular. The increasing number of synchrotron radiation sources all over the world facilitates the access to high-brilliance tunable X-rays. The experimental effort for XMCD experiments is moderate: For total yield detection of the absorption, simply the sample drain current is measured using a standard electrometer. The magnetic signal arises at atomic core level absorption edges, and is therefore element-specific, which allows the discrimination of magnetic properties of different atomic species in compounds or alloys, or the separate determination of contributions from different layers in multilayered magnetic structures. Finally, the so-called sum rules, proposed in 1992 and 1993 [2,3], allow the quantitative evaluation of magnetic moments, separated into spin and orbital contributions, from integrals over XMCD spectra.

It was also about a decade ago when it was realized that XMCD provided a very convenient contrast mechanism for magnetic imaging [4]. Since then quite a number of studies have been performed by either electron-optic imaging of the photoemitted electrons in a photoelectron emission microscope (PEEM) [5–23] or by X-ray imaging in an X-ray microscope [24–28]. Taking advantage of the element-selectivity, magnetic imaging using XMCD as contrast mechanism offers the unique possibility to obtain layer-resolved domain images of magnetic multilayered samples, if different elements are used in different magnetic layers. This allows to identify micromagnetic contributions to the coupling between magnetic layers that are separated by a non-magnetic spacer layer, a field receiving highest attention due to prospects of technological applications using magnetoresistive effects in such systems.

For the imaging of magnetic domains, the full spectroscopic information of XMCD is not necessary so that it is sufficient to tune the photon energy to a value where the magnetic contrast becomes maximum. Going one step further, it is also possible to combine spectroscopic and microscopic information in a more complete sense by performing full image microspectroscopic measurements to obtain the complete spectroscopic information of XMCD with microscopic lateral resolution [29–34].

In the present contribution, some of the unique features of XMCD are reviewed. Emphasis will then be laid on XMCD microscopy and microspectroscopy using PEEM. The following section provides an introduction into the basics of XMCD. It presents the sum rules in a simple and illustrative way, and discusses the role of orbital magnetic moments. In Section 3, some experimental results of layer-resolved magnetic domain imaging by XMCD-PEEM are presented. In Section 4, the use of XMCD-PEEM for the microscopic determination of magnetic moments is demonstrated. Section 5 provides an outlook.

2. Basics

2.1. *X-ray absorption spectroscopy*

The X-ray absorption spectra of transition metal ferromagnets are governed by resonances that occur if core electrons are excited into unoccupied 3d valence states just above the Fermi level. In the following, the discussion will be limited to the absorption at the $L_{2,3}$ lines of 3d transition metals. A more general comprehensive treatment of X-ray absorption spectroscopy can be found in Ref. [35]. Figure 1 illustrates the structure of an absorption spectrum of the $L_{2,3}$ absorption edge, i.e., the transition of 2p core electrons into unoccupied states above the Fermi level. The left upper panel shows a schematic representation of the occupied density of states of the 2p core levels. The important point here is the splitting of the 2p states into separate $2p_{1/2}$ and $2p_{3/2}$ levels by the spin–orbit interaction. The different height of the bars represents the different occupation numbers of the $2p_{1/2}$ and $2p_{3/2}$ levels, namely 2 and 4, respectively. The shape of the absorption spectrum is further determined by the unoccupied density of states available for transitions of electrons from these core states. The density of states around the Fermi energy is schematically shown in the upper right panel, where the shaded area represents the unoccupied states. The con-

*e-mail: kuch@mpi-halle.de

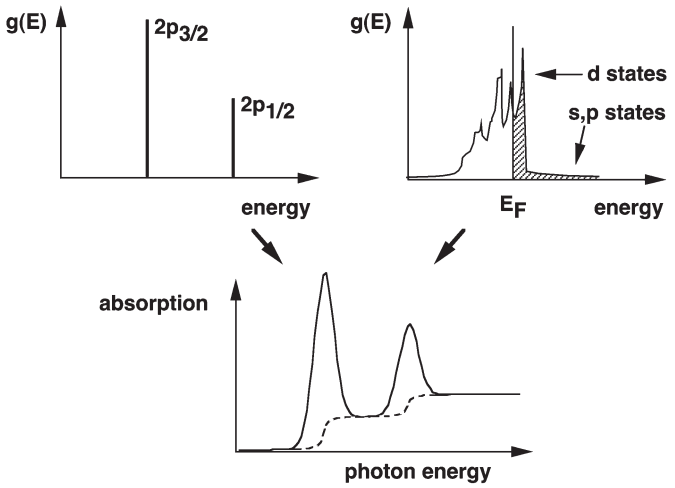

Fig. 1. Schematic illustration of X-ray absorption spectroscopy. The example shows absorption at the $L_{2,3}$ edges of a 3d transition metal. The absorption spectrum shown in the bottom panel results from the convolution of the occupied density of states of the 2p core levels (upper left) and the unoccupied density of states $g(E)$ of the valence states (upper right, shaded area). The contribution from s, p states is usually approximated and subtracted in the form of a step function (bottom panel).

tribution from states of predominantly s, p character is represented by a flat energy dependence, whereas d states show up as sharp peaks close to E_F. The resulting absorption spectrum is obtained from the convolution of the occupied density of states of the upper left panel and the unoccupied density of states of the upper right panel. Finite experimental photon energy resolution and lifetime broadening have to be taken into account by an additional convolution with a Gaussian energy distribution. A typical resulting $L_{2,3}$ absorption spectrum is shown in the bottom panel of Fig. 1 (continuous line). It is seen that the absorption signal related to transitions into empty 3d states shows up as two peaks at the energetic positions of the $2p_{1/2}$ and $2p_{3/2}$ states, whereas the unoccupied s, p states give rise to a step-like background. Since the magnetic moment of the 3d transition metals is mainly governed by 3d valence electrons, the latter is usually subtracted as a step-function with relative step heights of 2:1 [36], according to the occupation of the $2p_{3/2}$ and $2p_{1/2}$ core states, as shown in the bottom panel of Fig. 1 (dashed line).

2.2. *Magnetic circular dichroism*

In Fig. 1 no distinction of the direction of electron spin was done. The density of the valence states of a ferromagnet exhibits different density of states for electrons of majority and minority spin. The exchange interaction in the valence states leads to an energetic shift between these two partial densities of states and hence to a spin polarization of the unoccupied states. In the 3d transition metal ferromagnets these are mainly the 3d states which gives rise to a spin magnetic moment defined by the difference in occupation.

If $2p \rightarrow 3d$ transitions are excited by circularly polarized radiation, these transitions exhibit a spin polarization because of transition selection rules [37,38]. For a certain light helicity, more electrons of one spin direction with respect to the direction of the incoming light are excited into the unoccupied 3d states than of the other spin direction with the quantization axis along the direction of the light helicity vector. This spin polarization exhibits opposite sign for $2p_{3/2} \rightarrow 3d$ and for $2p_{1/2} \rightarrow 3d$ transitions. In a paramagnet this does not lead to a change in absorption intensity, since the number of unoccupied states is equal for both spin directions. In a ferromagnet, however, the absorption in the range of $2p \rightarrow 3d$ transitions will depend on the relative orientation of the spin polarization of the empty valence states and the spin polarization of the electronic transitions. If they are aligned and both spin polarizations coincide in sign, the transition probability, and hence, the X-ray absorption will be higher than for opposite sign. In a dichroism spectrum calculated as the difference between absorption spectra for opposite helicity, a non-zero difference will show up at the energy positions of the peaks related to transitions from the $2p_{3/2}$ and $2p_{1/2}$ levels into the empty 3d-like states. Figure 2 shows as an example the magnetic circular dichroism spectrum of an ultrathin Co film. In the upper panel, Fig. 2(a), the absorption spectra in the photon energy range of the Co $2p \rightarrow 3d$ transitions are shown for right and left circularly polarized light. For a fixed sample magnetization the absorption at the L_3 peak (corresponding to $2p_{3/2} \rightarrow 3d$ transitions) is higher for right circular polarization (continuous line) compared to left circular polarization (dashed line), while the situation is opposite at the L_2 peak ($2p_{1/2} \rightarrow 3d$ transitions). The bottom panel, Fig. 2(b), shows the difference between the two curves of panel (a). It displays the dichroism, which shows up with different sign at the two Co absorption edges.

2.3. *The sum rules*

The known spin polarization of the $2p \rightarrow 3d$ transitions resulting from selection rules can be used as a probe to

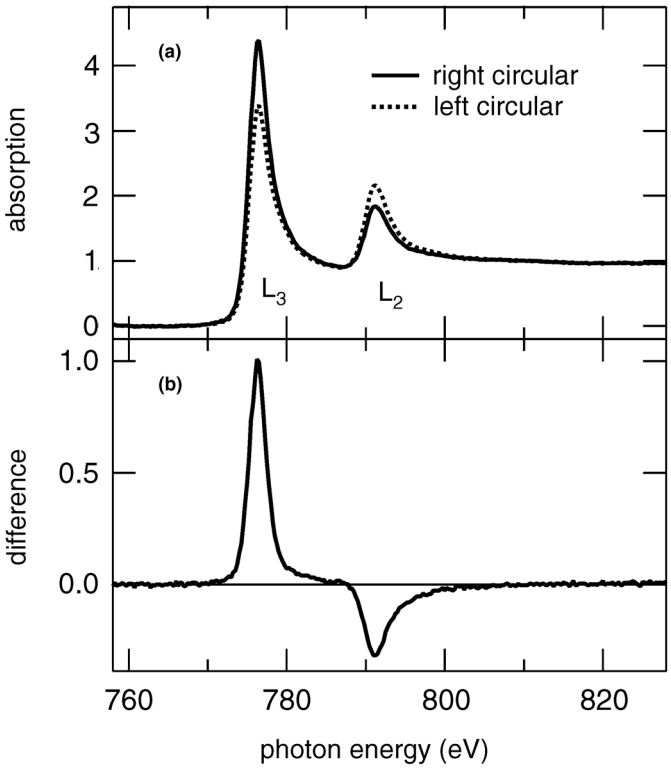

Fig. 2. Example of an experimental XMCD spectrum of a thin Co film on Cu(001). (a): Absorption spectra at the Co $L_{2,3}$ edge for right circular (continuous line) and left circular polarization (dotted line) of the exciting X-rays. (b): Difference between the two spectra of (a).

quantitatively measure the spin polarization of the unoccupied valence density of states, which is directly connected with the spin magnetic moment. In addition to the spin polarization, $2p \rightarrow 3d$ transitions excited by circularly polarized light also exhibit a polarization with respect to the orbital electron momentum. This is a direct consequence of the absorption of a circularly polarized photon with angular momentum $\Delta m = \pm 1$ [38,39]. Both, the $2p_{1/2} \rightarrow 3d$ and $2p_{3/2} \rightarrow 3d$ transitions, show the same sign and same magnitude of orbital polarization, while the spin polarization of the $2p_{1/2} \rightarrow 3d$ transitions is opposite and twice the spin polarization of the $2p_{3/2} \rightarrow 3d$ transitions. Because of the different behavior of the sign at the L_3 and the L_2 edge, the contributions from spin and orbital magnetic moments define an orthonormal basis for a measured XMCD spectrum. It can be used to decompose a signal into its spin and orbital components, which is exactly what is described by the sum rules. An illustrative explanation is given in Fig. 3. In a first step, the (hypothetical) cases of samples with either only an orbital magnetic moment or only a spin magnetic moment should be considered. The XMCD spectra that would result from such samples are schematically depicted in panels (a) and (b), respectively. Panel (a) shows the difference spectrum upon light helicity reversal of a sample with an orbital, but no spin magnetic moment. If a sample possesses a non-zero orbital magnetic moment this means that the unoccupied states (and also the occupied states) have a non-zero net angular momentum. Since the orbital polarization of the electronic transitions into these states is equal at the two edges, the difference curve exhibits two peaks in the same direction, the peak at L_3 being twice as high as the one at L_2 because of the higher intensity related to the different occupation of the 2p core states. Panel (b) shows the schematic XMCD difference spectrum for a sample with only a spin magnetic moment, and no orbital moment. In this case, peaks of opposite sign are encountered at the two edges. The higher spin polarization of transitions from the L_2 edge compensates its lower intensity, so that both peaks exhibit equal height.

A spectrum of a real sample with both, spin and orbital magnetic moments, would be a linear superposition of both spectra, as shown schematically in panel (c). Any such experimental spectrum can be decomposed unambiguously into its spin and orbital basis functions to obtain the spin and orbital moments. This is quantitatively described by the sum rules. If we denote the areas of the difference peaks by A and B, as indicated in Fig. 3(c), the orbital and spin moments μ_L and $\mu_{S,eff}$ can be obtained by

$$\mu_L = -\frac{2}{3C}(A + B)\mu_B, \tag{1}$$

$$\mu_{S,eff} = -\frac{1}{C}(A - 2B)\mu_B. \tag{2}$$

These equations are often called the first and second sum rule. They assume complete circular polarization of the exciting X-rays and full alignment between helicity vector and sample magnetization; the numbers that are obtained have, therefore, to be corrected for incomplete circular polarization and for the angle between light propagation

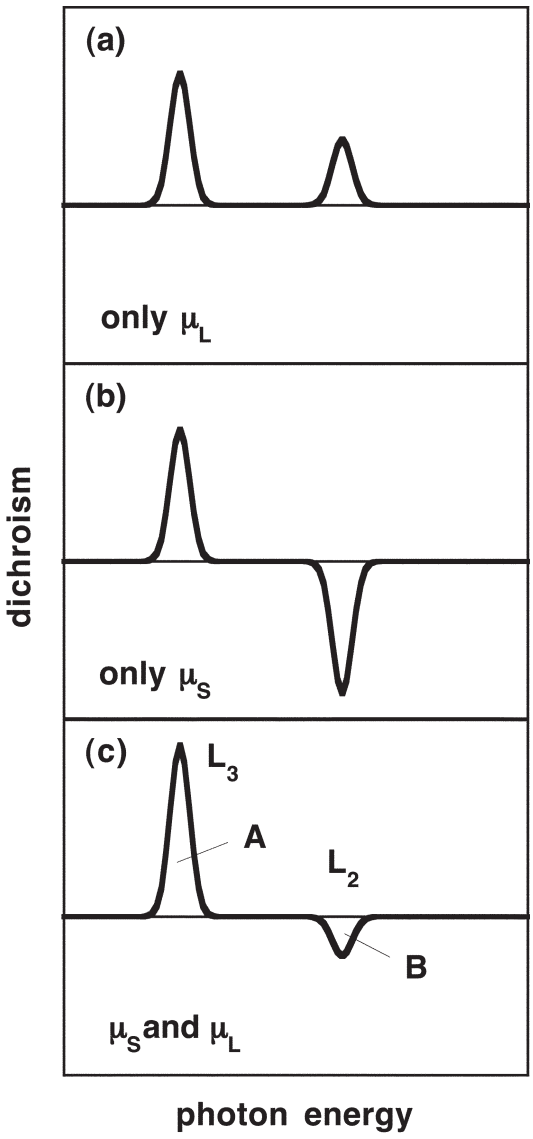

Fig. 3. Schematic illustration of the separation of spin and orbital magnetic moments from XMCD spectra. (a) XMCD difference spectrum of a sample with only an orbital magnetic moment, (b) XMCD difference spectrum of a sample with only a spin magnetic moment, (c) XMCD difference spectrum of a sample with both spin and orbital magnetic moments.

and sample magnetization. The constant C can be in general determined from a reference measurement of a sample with known moments. It is more common, however, to use the relation between the helicity-averaged integrated intensity under the absorption curves and the number of holes in the 3d valence band n_h in order to determine C:

$$n_h = \frac{1}{C}(I(L_2) + I(L_3)). \tag{3}$$

Here, $I(L_2)$ and $I(L_3)$ denote the integrals of the L_2 and L_3 peaks in the absorption spectrum, after subtraction of the s, p background as sketched in Fig. 1. If reasonable assumptions for the number of valence band holes can be made, it is thus possible to obtain spin and orbital moments from a single XMCD experiment without any reference measurements.

It has to be mentioned that the "spin moment" extracted from the sum rules is an effective spin moment $\mu_{S,eff}$ [3], which includes the actual spin magnetic moment μ_S plus a

contribution from the magnetic dipole term T_Z, $\mu_{S,eff} = \mu_S + (7/2)T_Z$. The latter is zero in the bulk of cubic crystals, but can be of the same order as the orbital moment in ultrathin films [40].

It should be noted that the sum rules are based on several simplifications. Transitions are considered to take place between electronic states of free atoms. A complete energetic separation of $2p_{1/2}$ and $2p_{3/2}$ states is necessary to obtain the integrals A and B correctly. This is particularly difficult for the less than half filled 3d transition metals. Furthermore, many-particle effects are neglected. A number of studies has thus been devoted to explore the validity of the sum rules. Although there has been some dispute [36,41–45], they seem to yield reasonable results for spin and orbital moments, at least for the more than half filled 3d transition metals [36,41,46–48]. The interested reader is referred to Refs. [38,39,41,49–51] for more comprehensive reviews.

2.4. *Orbital magnetic moments*

After the proposal of the XMCD sum rules not only the spin or total magnetic moment, but also the orbital magnetic moment became easily accessible to experiment. As a consequence the interest has also focussed on the latter. Although comparably small in solids, the orbital moment is linked to interesting physical properties. It had been first discussed by Bruno in 1989 that the magneto-crystalline anisotropy, that is the variation of total energy with the angle of magnetization in a crystalline lattice, is related to the anisotropy of the orbital magnetic moment [52]. The orbital moment should be higher for an energetically preferred direction of magnetization [53–55]. This relation had been experimentally confirmed by several groups by measurements on Co/Au(111) [40], Co/Pt multilayers [56], Co/Ni/Cu(001) [30,57] and Ni/Pt multi-layers [58]. It opened the possibility of determining the angular dependence of the magnetic anisotropy energy in an element-selective way by measuring the orbital magnetic moment by XMCD.

Another aspect of the orbital moment is its sensitivity to the dimensionality of the system. Increased orbital moments have been observed for decreasing thickness of a ferromagnetic film using ultrathin Co overlayers on Cu(001) [59], Co/Pd multilayers [60,61], Co/Pt multilayers [60], Fe/Pd multilayers [47] and in artificially ordered FeCu compounds [62,63]. Going one step further from two dimensions to one or zero dimensions, even more drastic enhancements of the orbital moment have been observed recently [64,65].

It is obvious from these examples that the quantitative determination not only of the spin magnetic moment, but also of the orbital moment of ultrathin films and magnetic nanostructures is one of the most valuable features of XMCD. However, the analysis of the experiments has to be carried out very carefully in order to extract meaningful numbers. While the result from the sum rules for the spin moment is more robust against experimental artifacts, the value of the orbital moment is quite sensitive to small data distortions. One example is saturation effects in the total electron yield mode of detection, which arise if the intensity of the X-ray wave is not constant within the volume probed by the electron escape depth [66,67]. They become more serious for thicker films or semi-infinite samples, and for more grazing angles of incidence. The error induced by saturation effects is much higher in the orbital moment than in the spin moment [67]. If this is kept in mind, the determination of orbital moments by XMCD can be used as a powerful tool for the investigation of magnetic properties in ultrathin magnetic films and at surfaces.

3. Layer-resolved magnetic domain imaging by XMCD-PEEM

Several advantages can be listed for using XMCD as contrast mechanism for magnetic imaging, the most important one, however, is the intrinsic element sensitivity of XMCD for investigations of systems relevant for magnetoresistive applications. A common feature of all systems for which giant magnetoresistive effects are observed, is that they contain two or more magnetic layers within a multi-layered thin film structure, and that the magnetization of these layers has to be controlled independently. XMCD-based imaging techniques provide the unique opportunity to image each magnetic layer in such multilayered magnetic systems separately provided they contain different elements. The principle and an example of layer-resolved magnetic imaging by XMCD-PEEM will be presented in this section.

Figure 4 explains schematically the principle of layer-resolved magnetic imaging by XMCD-PEEM. A multi-layered sample containing two different magnetic layers, here a Ni and a Co layer, is illuminated by circularly polarized X-rays. If the photon energy is tuned to the maximum of the elemental absorption edge of one of the two layers, the X-ray absorption within that layer exhibits a non-vanishing difference upon helicity reversal which reflects the magnetic domain structure of that layer.

The imaging process is indicated in Fig. 4 by the long vertical arrows. The photoelectron emission microscope uses the photoemitted low energy secondary electrons to create a magnified image of the sample. The magnetic dichroism will thus directly show up in the image intensity

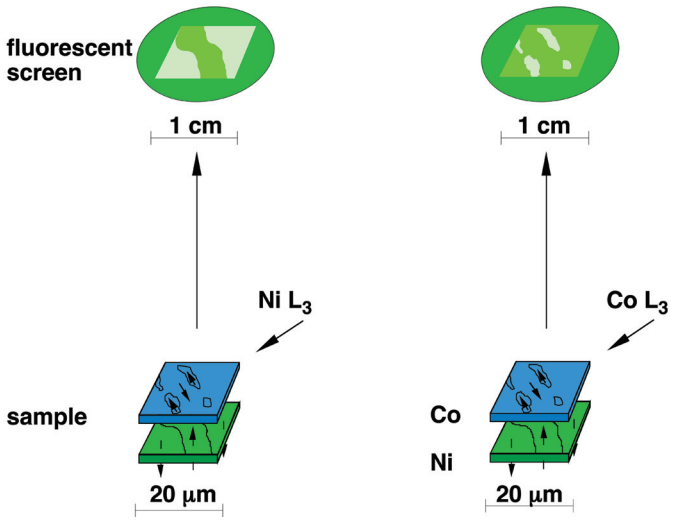

Fig. 4. Schematic working principle of layer-resolved magnetic domain imaging using XMCD as magnetic contrast mechanism. Each layer of a multilayered magnetic sample which contains different elements can be viewed separately by imaging the X-ray absorption distribution in the sample and tuning the photon energy to the respective absorption edges.

recorded on a fluorescent screen, as schematically indicated in Fig. 4.

Photoelectron emission microscopy actually belongs to the oldest electron microscopes that have been realized [68,69]. The word "photoelectron" in the name is of historic nature and a bit confusing for synchrotron radiation usage of PEEM, since here mainly inelastic secondary electrons are detected. A recent review about photoelectron emission microscopy can be found in Ref. [16]. When PEEM is used for the imaging of XMCD, the intensity of absorption is detected by the intensity of photoexcited electrons. Electrons from buried layers are thereby detected after attenuation upon transversing the overlayers. A typical attenuation length for 3d ferromagnets is about 2 nm [67]. Electrons emitted in overlayers of different elements do not contribute to the dichroism, since their intensity stays constant upon helicity reversal.

The sample schematically indicated in Fig. 4 contains Co and Ni magnetic layers. If these layers are epitaxially stabilized in a tetragonally distorted fcc structure with the lateral lattice constant of Cu(001), the preferred magnetization direction of Ni is along the film normal [70–72], whereas Co is magnetized in the film plane along ⟨110⟩ crystallographic directions [73,74]. For oblique incidence of the circularly polarized X-rays, as indicated by arrows in Fig. 4, both, in-plane and out-of-plane magnetization domain patterns exhibit a non-vanishing projection on the light incidence direction and thus a magnetic circular dichroism. A magnified image of the lateral absorption distribution at the respective elemental absorption edges will display the magnetic domain pattern as intensity distribution according to the projection of the local magnetization vector in the domains onto the light incidence direction. If it is possible to rotate the sample about its surface normal, the behavior of the magnetic contrast upon such an azimuthal rotation of the sample can be used for a vectorial determination of the local magnetization directions [17,18].

Practically, the absorption difference upon helicity reversal is presented as domain image in order to cancel all non-magnetic contributions. An example of an XMCD-PEEM image of a Co/Cu/Ni trilayer on Cu(001) is shown in Fig. 5. The images were taken after depositing the films in zero magnetic field. A sketch of the sample indicating the thickness of the different layers in atomic monolayers (ML) is given at the bottom. At the present thickness of the non-magnetic Cu spacer layer, the two magnetic layers are only weakly coupled by indirect exchange interaction [75,76]. The magnetization directions of the Co and Ni layers will thus take on a non-collinear configuration in which each layer is magnetized along its preferred direction, as indicated in the sketch. The Ni domain image as obtained from the XMCD at the maximum of the Ni L_3 absorption is shown on the left. It displays a stripe-like domain of opposite perpendicular magnetization, as indicated. The right image shows the Co domain pattern at the same sample position. A higher number of smaller domains compared to the Ni image is observed here, in which the local magnetization direction is pointing along the four in-plane ⟨110⟩ directions, indicated by arrows in some domains. For the mutual perpendicular arrangement of the magnetization directions in the two magnetic layers in

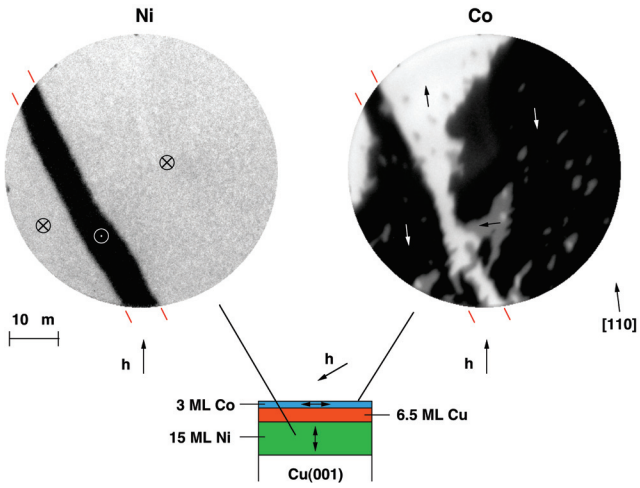

Fig. 5. Example of layer-resolved magnetic domain images by XMCD-PEEM. Presented are images of a 3 ML Co/6.5 ML Cu/15 ML Ni trilayer on a Cu(001) single crystal surface (ML = atomic monolayer). Left: domain image of the Ni layer, acquired at the Ni L_3 edge, right: domain image of the Co layer, acquired at the Co L_3 edge. The magnetization directions in the two layers are orthogonal to each other because of magnetic anisotropies, as indicated in the sketch. In spite of these mutually perpendicular magnetization directions some correlation in the two domain images is recognized. Small black lines outside the images indicating identical positions aid to recognize this.

that sample one would not necessarily expect a correlation of the domain patterns. By looking at the two images in Fig. 5 carefully, one realizes that at about 50% of the domain boundaries of the Ni image, indicated by small black lines outside the images, also domain boundaries of the Co layer are located. This is an indication of the influence of local magnetic stray fields emanating from domain walls, which lead to a local coupling between the two layers [23]. The detailed analysis of such measurements is expected to significantly further our understanding of the micromagnetic coupling mechanisms between ultrathin magnetic films, a subject that is at the leading edge of current magnetic thin film research.

4. XMCD microspectroscopy

In order to make the full spectroscopic information inherent to XMCD available for microscopy, images of the absorption distribution have to be acquired at each step during a scan of the photon energy for both helicities. In such a three-dimensional stack of images, each image pixel can be treated and analyzed as a complete XMCD spectrum. Certain details have to be taken into account for a quantitative analysis of such microspectroscopic data sets, as outlined in Refs. [32,34]. One example is the normalization of the local photon flux by an integral beam intensity monitor. If this is done carefully, such XMCD microspectroscopic measurements can provide valuable information about spin and orbital magnetic moments on a microscopic scale after pixel-by-pixel sum rule analysis. An example is given in Fig. 6 for a Ni/Fe/Co trilayer on Cu(001). Ultrathin Fe films grown with the lateral lattice constants of Cu(001) acquire the magnetically interesting fcc structural phase [77–80]. The 6 ML Co bottom layer was introduced to make sure that the ordering temperature of the Fe layer was high enough, and to force the

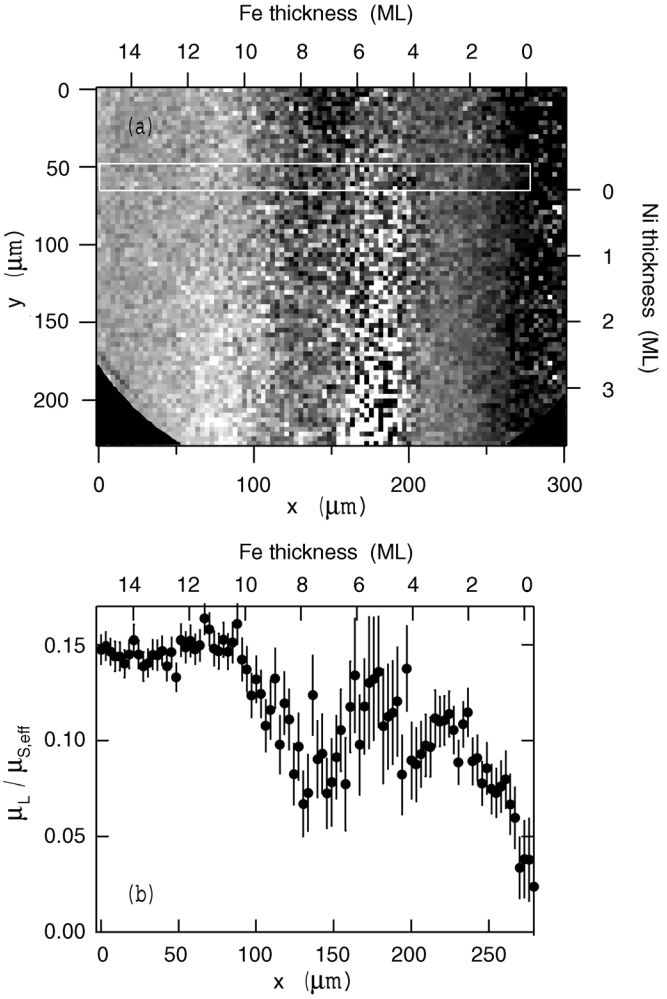

Fig. 6. Example of XMCD microspectroscopy data yield from XMCD-PEEM. (a): Map of orbital to effective spin moment ratio in a Ni/Fe crossed double wedge on 6 ML Co/Cu(001). Fe and Ni thicknesses are given at the upper and right axes, respectively. (b): Ratio of orbital to effective spin moment measured with a line scan along the white rectangle shown in (a).

magnetization direction into the film plane. Fe and Ni were deposited as crossed micro-wedges as explained in Ref. [31] to facilitate the study of thickness dependent properties. For the analysis of the many thousand single pixel XMCD spectra, an automatic fitting procedure was used as described in Refs. [32,34]. It compares the local XMCD spectra to a reference XMCD spectrum obtained from an average within a certain region of the image.

Figure 6(a) shows a map of the ratio of orbital to effective spin moment of Fe after correcting saturation effects. The Fe thickness increases from right to left, as indicated at the top axis. The start of the Ni wedge and the Ni top layer thickness are indicated at the right axis, but are of minor importance here. A more detailed discussion is found in Ref. [31]. A discontinuous variation of the orbital to spin moment ratio is observed as a function of Fe layer thickness. Figure 6(b) shows a line scan of this ratio along the length of the white rectangle in panel (a), averaging over its width. The general trend in this data is that thinner Fe layers show a decreased orbital moment, contrary to the simple argument of reduced dimensionality. In the present example, also the element-resolved magnetic anisotropy of ultrathin fcc Fe layers has to be considered, which favors an out-of-plane magnetization direction. The Fe layer in the present example is thus magnetized in a less preferred direction by the proximity of the Co layer, which may explain the reduced orbital moment at low Fe thicknesses [31].

5. Outlook

The data presented above show that the combination of XMCD and microscopy represents a very powerful method for studying quantitative magnetic properties of most of the relevant and interesting systems in current magnetism research. Future improvements concerning the brightness of the illumination and the efficiency of the detection system should reduce the noise level of the microspectra and allow to probe magnetic anisotropy at the microscopic level, e.g., in domain walls, or in technologically relevant magnetic microstructures. The development of new PEEM instruments with aberration-correcting optics [81] can push the limit for the attainable maximum resolution. Layer selective magnetic imaging and microspectroscopy with spatial resolution down to 2 nm can be foreseen in the near future. The inclusion of time-resolved stroboscopic pump-probe experiments which exploit the pulsed time structure of synchrotron radiation [82] into XMCD-PEEM micro-spectroscopy will open the way for the quantitative investigation of magnetization dynamics on microscopic lengthscales. Snapshots of the spatial spin and orbital magnetic moments' distribution in the course of reversible dynamic magnetization processes may be obtained in that way.

Acknowledgments

The author would like to thank X. Gao, J. Gilles, J. Kirschner, S. Imada, and S. Suga for collaboration in the experiments presented in Sections 3 and 4. and B. Zada for technical assistance. Help and support by W. Mahler and the BESSY staff (Section 3) as well as Y. Saitoh and the SPring-8 staff (Section 4) during the beamtimes is gratefully acknowledged. This work is supported by the German Minister for Education and Research (BMBF) under grant Nos. 05 SL8EF19 and 05 KS1EFA6. Further financial support from DFG (Nos. Ki 358/3-1 and 446 JAP-113/179/0), JSPS, and JASRI is also gratefully acknowledged.

References

1. Schütz, G. *et al.*, Phys. Rev. Lett. **58**, 737 (1987).
2. Thole, B. T., Carra, P., Sette, F. and van der Laan, G., Phys. Rev. Lett. **68**, 1943 (1992).
3. Carra, P., Thole, B. T., Altarelli, M. and Wang, X., Phys. Rev. Lett. **70**, 694 (1993).
4. Stöhr, J. *et al.*, Science **259**, 658 (1993).
5. Schneider, C. M. *et al.*, in "Magnetic Ultrathin Films, Multilayers and Surfaces, 1997," (edited by J. Tobin *et al.*), (Materials Research Society, Pittsburgh, 1997).
6. Swiech, W. *et al.*, J. Electron Spectrosc. Relat. Phenom. **84**, 171 (1997).
7. Hillebrecht, F. U., Spanke, D., Dresselhaus, J. and Solinus, V. J., Electron Spectrosc. Relat. Phenom. **84**, 189 (1997).
8. Kuch, W. *et al.*, Surf. Rev. Lett. **5**, 1241 (1998).
9. Anders, S. *et al.*, Rev. Sci. Instrum. **70**, 3973 (1999).
10. Imada, S. *et al.*, Jpn. J. Appl. Phys. **39**, L585 (2000).
11. Thomas, L. *et al.*, Phys. Rev. Lett. **84**, 3462 (2000).
12. Nolting, F. *et al.*, Nature **405**, 767 (2000).
13. Kuch, W., Gao, X. and Kirschner, J., Phys. Rev. B **65**, 064406 (2002).
14. Kuch, W. *et al.*, Phys. Rev. B **65**, 140408 (2002).
15. Schneider, C. M. *et al.*, J. Magn. Magn. Mater. **233**, 14 (2001).

16. Schneider, C. M. and Schönhense, G., Rep. Prog. Phys. **65**, R1785 (2002).
17. Kuch, W., Gilles, J., Gao, X. and Kirschner, J., J. Magn. Magn. Mater. **242–245**, 1246 (2002).
18. Fukumoto, K., Daimon, H., Chelaru, L. I., Offi, F., Kuch, W. and Kirschner, J., Surf. Sci. **514**, 151 (2002).
19. Wu, Y. Z. *et al*., Phys. Rev. B **65**, 214417 (2002).
20. Choi, H. J. *et al*., Phys. Rev. B **66**, 014409 (2002).
21. Offi, F., Kuch, W., Chelaru, L. I., Kotsugi, M. and Kirschner, J., J. Magn. Magn. Mater. **261**, L1 (2003).
22. Offi, F. *et al*., Phys. Rev. B **67**, 094419 (2003).
23. Kuch, W., Appl. Phys. A **76**, 665 (2003).
24. Fischer, P., Schütz, G., Schmahl, G., Guttmann, P. and Raasch, D., Z. Phys. B: Condens. Matter **101**, 313 (1996).
25. Fischer, P. *et al*., Phys. D: Appl. Phys. **31**, 649 (1998).
26. Fischer, P. *et al*., Rev. Sci. Instrum. **72**, 2322 (2001).
27. Eimüller, T. *et al*., J. Appl. Phys. **89**, 7162 (2001).
28. Eimüller, T. *et al*., Appl. Phys. A **73**, 697 (2001).
29. Kuch, W. *et al*., J. Appl. Phys. **87**, 5747 (2000).
30. Kuch, W. *et al*., Phys. Rev. B **62**, 3824 (2000).
31. Kuch, W. *et al*., J. Electron Spectrosc. Relat. Phenom. **109**, 249 (2000).
32. Kuch, W. *et al*., Surf. Sci. **480**, 153 (2001).
33. Imada, S., Suga, S., Kuch, W. and Kirschner, J., Surf. Rev. Lett. **9**, 877 (2002).
34. Kuch, W., in: *Magnetic Microscopy of Nanostructures*, edited by H. Hopster and H. P. Oepen, (Springer, Berlin), in print.
35. Stöhr, J., *NEXAFS Spectroscopy*, (Springer, Berlin, 1996).
36. Chen, C. T. *et al*., Phys. Rev. Lett. **75**, 152 (1995).
37. Fano, U., Phys. Rev. A **178**, 131 (1969).
38. Ebert, H., Rep. Prog. Phys. **59**, 1665 (1996).
39. Ebert, H., in *Spin–Orbit-Influenced Spectroscopies of Magnetic Solids*, edited by H. Ebert and G. Schütz (Springer, Berlin, 1996).
40. Weller, D. *et al*., Phys. Rev. Lett. **75**, 3752 (1995).
41. Idzerda, Y. U., Chen, C. T., Lin, H.-J., Tjeng, H. and Meigs, G., Physica B **208–209**, 746 (1995).
42. Wu, R. and Freeman, A. J., Phys. Rev. Lett. **73**, 1994 (1994).
43. O'Brien, W. L., Tonner, B. P., Harp, G. R. and Parkin, S. S. P., J. Appl. Phys. **76**, 6462 (1994).
44. Rioux, D., Allen, B., Höchst, H., Zhao, D. and Huber, D. L., Phys. Rev. B **56**, 753 (1997).
45. Schwitalla, J. and Ebert, H., Phys. Rev. Lett. **80**, 4586 (1998).
46. Vogel, J. and Sacchi, M., Phys. Rev. B **49**, 3230 (1994).
47. Le Cann, X., Boeglin, C., Carrière, B. and Hricovini, K., Phys. Rev. B **54**, 373 (1996).
48. Hunter Dunn, J., Arvanitis, D. and Mårtensson, N., Phys. Rev. B **54**, R11 157 (1996).
49. Stöhr, J., J. Electron Spectrosc. Relat. Phenom. **75**, 253 (1995).
50. Stöhr, J., Padmore, H. A., Anders, S., Stammler, T. and Scheinfein, M. R., Surf. Rev. Lett. **5**, 1297 (1998).
51. Stöhr, J. and Nakajima, R., IBM J. Res. Develop. **42**, 73 (1998).
52. Bruno, P., Phys. Rev. B **39**, 865 (1989).
53. Stöhr, J. and König, H., Phys. Rev. Lett. **75**, 3748 (1995).
54. Dürr, H. A. and van der Laan, G., Phys. Rev. B **54**, R760 (1996).
55. van der Laan, G., J. Phys.: Cond. Matt. **10**, 3239 (1998).
56. Dürr, H. A. and van der Laan, G., J. Appl. Phys. **81**, 5355 (1997).
57. Dürr, H. A. *et al*., Science **277**, 213 (1997).
58. Wilhelm, F. *et al*., Phys. Rev. B **61**, 8647 (2000).
59. Tischer, M. *et al*., Phys. Rev. Lett. **75**, 1602 (1995).
60. Weller, D. *et al*., Phys. Rev. B **49**, 12888 (1994).
61. Wu, Y., Stöhr, J., Hermsmeier, B. D., Samant, M. G. and Weller, D., Phys. Rev. Lett. **69**, 2307 (1992).
62. Kuch, W. *et al*., J. Appl. Phys. **83**, 7019 (1998).
63. Kuch, W. *et al*., Phys. Rev. B **58**, 8556 (1998).
64. Gambardella, P. *et al*., Nature **416**, 301 (2002).
65. Gambardella, P. *et al*., Phys. Rev. Lett. **88**, 047202 (2002).
66. Hunter Dunn, J. *et al*., J. Phys.: Cond. Matt. **7**, 1111 (1995).
67. Nakajima, R., Stöhr, J. and Idzerda, Y. U., Phys. Rev. B **59**, 6421 (1999).
68. Brüche, E., Z. Phys. **86**, 448 (1933).
69. Pohl, J., Zeitschr. f. technische Physik **12**, 579 (1934).
70. O'Brien, W. L. and Tonner, B. P., Phys. Rev. B **49**, 15 370 (1994).
71. Schulz, B. and Baberschke, K., Phys. Rev. B **50**, 13467 (1994).
72. Farle, M., Mirwald-Schulz, B., Anisimov, A. N., Platow, W. and Baberschke, K., Phys. Rev. B **55**, 3708 (1997).
73. Krams, P., Lauks, F., Stamps, R. L., Hillebrands, B. and Güntherodt, G., Phys. Rev. Lett. **69**, 3674 (1992).
74. Kowalewski, M., Schneider, C. M. and Heinrich, B., Phys. Rev. B **47**, 8748 (1993).
75. *Ultrathin Magnetic Structures*, edited by B. Heinrich and J. A. C. Bland, (Springer, Berlin, 1994), **2**, Chap. 2.
76. Stiles, M. D., J. Magn. Magn. Mater. **200**, 322 (1999).
77. Gradmann, U., in *Handbook of Magnetic Materials*, edited by K. H. J. Buschow (Elsevier, Amsterdam, 1993).
78. Bayer, P., Müller, S., Schmailzl P. and Heinz, K., Phys. Rev. B **48**, 17611 (1993).
79. Müller, S., Bayer, P., Kinne, A., Schmailzl P. and Heinz, K., Surf. Sci. **322**, 21 (1995).
80. Müller, S. *et al*., Phys. Rev. Lett. **74**, 765 (1995).
81. Fink, R., *et al*., J. Electron Spectrosc. Relat. Phenom. **84**, 231 (1997).
82. Vogel, J. *et al*., Appl. Phys. Lett. **82**, 2299 (2003).

